

A large, chemically enriched, neutral gas reservoir in a galaxy at $z = 6.782$ [★]

A. Saccardi^{1,★★}, S. D. Vergani^{2,3}, L. Izzo^{4,5}, V. D’Elia⁶, K. E. Heintz^{5,7,8}, A. De Cia⁹, D. B. Malesani^{5,7,10}, J. T. Palmerio¹, P. Petitjean³, S. Savaglio^{11,12,13}, N. R. Tanvir¹⁴, R. Salvaterra¹⁵, R. Brivio¹⁶, S. Campana¹⁶, L. Christensen^{5,7}, S. Covino¹⁶, J. P. U. Fynbo^{5,7}, D. H. Hartmann¹⁷, C. Konstantopoulou⁸, A. J. Levan^{10,18}, A. Martin-Carrillo¹⁹, A. Melandri²⁰, L. Piro²¹, G. Pugliese²², P. Schady²³, B. Schneider²⁴

(Affiliations can be found after the references)

ABSTRACT

The physical and chemical characterization of galaxies formed within the first billion years after the Big Bang remains one of the central goals in contemporary astrophysics. For the last two decades, optical and near-infrared spectroscopy of long gamma-ray bursts (GRBs) have been heralded as an effective diagnostic to probe the interstellar medium (ISM) of the galaxies hosting these events and their metal and dust content, reaching even the most distant redshifts.

An opportunity to fulfill this expectation was provided by the recent blast triggered by the *Neil Gehrels Swift Observatory* of GRB 240218A at redshift $z = 6.782$. From the GRB explosion, we could study a high-redshift galaxy selected in a complementary way with respect to flux-limited surveys, not depending on galaxy luminosity and stellar mass. Furthermore, the GRB afterglow allows us to perform a coring of the galaxy ISM and to determine its kinematic and chemical properties. We present the VLT/X-shooter spectrum of its afterglow enabling the detection and the detailed characterization of neutral-hydrogen, low-ionization, high-ionization and fine-structure absorption lines, as well as excited level transitions. From this rich variety of absorption lines associated with gas inside and around the GRB host galaxy, we determine the metallicity, kinematics, chemical abundance pattern and dust depletion. This provides the first detailed characterization of the neutral gas of a galaxy at $z > 6.5$.

Thanks to the presence of fine-structure absorption lines we could estimate the distance of the closest absorbing gas clouds as $d_{II} = 620^{+230}_{-140}$ pc. We determine a high neutral hydrogen column density, $\log(N(\text{H I})/\text{cm}^{-2}) = 22.5 \pm 0.3$, which is the highest one at $z \gtrsim 6$ determined so far for a GRB host galaxy, as well as a surprisingly high metal column density, $\log(N(\text{Zn II})/\text{cm}^{-2}) > 14.3$. The observed metallicity of the host galaxy system is $[\text{Zn}/\text{H}] > -0.8$. Taking the derived column densities at face value, although a number of transitions are saturated, we find evidence of a high amount of dust depletion and of peculiar nucleosynthesis, with an overabundance of aluminum, as in other high-redshift GRB host galaxies at $z \sim 6$.

The high hydrogen column density, metal abundances and dust depletion in the neutral gas align with those of the ionized gas of very high-redshift galaxies unveiled by ALMA and JWST, testifying that a rapid build up of metals and dust, and massive neutral hydrogen reservoirs seem to be common features of galaxies in the early Universe. This research highlights the remarkable potential of GRBs as tools to investigate the detailed properties of galaxies deep into the reionization epoch, and stresses the importance of new missions capable to enlarge the sample of very high-redshift GRBs.

Key words. Gamma-ray burst: general - Gamma-ray burst: individual : GRB 240218A – Galaxies: abundances – Galaxies: ISM - ISM: dust, extinction - Galaxies: high-redshift

1. Introduction

Unveiling galaxies at the highest redshifts and studying their chemical evolution is a key objective in modern astrophysics.

Neutral gas, primarily composed of atomic hydrogen (H I), is a fundamental component of the interstellar medium (ISM) and the circumgalactic medium (CGM) in galaxies, and contains the majority of metals at $z \geq 2.5$ (Péroux & Howk 2020). Neutral gas forms the primary reservoir from which stars form and hence a key player in chemical enrichment. Therefore, its observation is fundamental to understand galaxy evolution (Madau & Dickinson 2014).

Nowadays, thanks to *James Webb* Space Telescope (JWST), it is possible to measure H I column densities in large fractions

in galaxies during the reionization epoch at $z > 5$ and out to $z \sim 14$ (Umeda et al. 2024; D’Eugenio et al. 2024; Hainline et al. 2024; Carniani et al. 2025; Witstok et al. 2025; Heintz et al. 2025). Through the detection of strong damped Lyman- α (DLA) absorbers, Heintz et al. (2024) provided direct measurements of H I for galaxies at $z > 9$, and showed evidence for abundant neutral gas reservoirs in some early galaxies. In order to sustain the high H I column densities while covering the entire physical extent of the galaxies, these sources must be embedded in large, extended layers or shells of neutral gas. High-redshift galaxies at $z > 6$ were not only forming stars efficiently but were also undergoing significant chemical evolution (Langeroodi et al. 2023; Heintz et al. 2023a; Nakajima et al. 2023; Curti et al. 2024), showing richness of spectral features and unusual chemical abundances (e.g. Bunker et al. 2023; Curti et al. 2025; Castellano et al. 2024; D’Eugenio et al. 2024), which may indicate rapid enrichment processes occurring during the earliest stages of galaxy formation. These findings challenge earlier models that suggested that metal enrichment and dust for-

[★] Based on observations carried out under ESO prog. ID 110.24CF.015 (PI: N. Tanvir) with the X-shooter spectrograph installed at the Cassegrain focus of the Very Large Telescope (VLT), Unit 3 – Melipal, operated by the European Southern Observatory (ESO) on Cerro Paranal, Chile.

^{★★} E-mail: andrea.saccardi@cea.fr

mation were slower processes that occurred after $z \sim 5$ (Madau & Dickinson 2014).

Despite this progress, a detailed study of chemical and kinematic properties of neutral gas remains difficult, even for JWST. The most powerful way to directly measure the properties of the neutral gas is through absorption lines detected in the spectrum of a bright background source, such as quasars (QSOs) and gamma-ray bursts (GRBs; Gehrels & Razzaque 2013). GRBs serve as cosmic beacons, that probe in great detail the star-forming galaxies that host them, which are often faint and missed by flux-limited observations, out to the highest redshifts. The association of long-GRBs (LGRBs) with massive stars (Hjorth et al. 2003; Woosley & Bloom 2006; Fruchter et al. 2006; Hjorth et al. 2012; Cano et al. 2017) means that they point directly to the sites of star formation enriching the Universe (Krogager et al. 2024), unlike the alignments of QSOs, and makes them especially suitable to investigate galaxies and star formation up to the early Universe. They have already been observed out to $z_{\text{spec}} = 8.23$ (GRB 090423A; Salvaterra et al. 2009; Tanvir et al. 2009) and $z_{\text{phot}} \simeq 9.4$ (GRB 090429B; Cucchiara et al. 2011), and they are expected to be observable even beyond (Campana et al. 2022; Kann et al. 2024).

Ground-based telescopes equipped with medium/high-resolution spectrographs allow us to dissect the light from GRB afterglows, revealing precise information about the chemical and physical properties of the absorbing gas in the host galaxy, in particular on the neutral gas and its components. Optical and near-infrared (NIR) absorption spectroscopy and the high spectral signal-to-noise ratio (SNR) provide valuable information on the neutral hydrogen column density (Selsing et al. 2019; Tanvir et al. 2019), the gas kinematics, and the distance of absorbing material from the GRB (Prochaska et al. 2006; Vreeswijk et al. 2007; D’Elia et al. 2009b), shedding light on the chemical properties of the ISM, metals, and dust content of their host galaxies up to the highest redshifts (Sparre et al. 2014; Hartoog et al. 2015; Saccardi et al. 2023). All of this can be done independently of the brightness of the host galaxies. Furthermore, thanks to Very Large Telescope (VLT) X-shooter follow-up and its much higher spectral resolving power, we can constrain the neutral gas-phase and chemical composition much more accurately than will ever be possible with JWST.

Several studies investigate the metallicity and dust content of GRB-selected star-forming galaxies from $z \sim 2$ up to $z > 6$ (e.g., Bolmer et al. 2019; Heintz et al. 2023b). These galaxies exhibit significant metal and dust production, highlighting a rapid build-up of these components in the early Universe. They also show a large scatter in the dust-corrected metallicities at a given redshift (De Cia et al. 2018; Heintz et al. 2023b; Konstantopoulou et al. 2024), which is not captured in most state-of-the-art galaxy evolution simulations (Yates et al. 2021), although there is broad agreement with the chemical enrichment as a function of cosmic time. Furthermore, these works reveal that the dust-to-metal ratio in these galaxies grows steadily with cosmic time, aligning with the predictions of earlier models, but suggesting faster dust production than previously assumed. Additionally, there is evidence for a correlation between metallicity and dust-to-metal ratio (De Cia et al. 2013), suggesting that these galaxies are significant contributors to the cosmic dust budget at high redshifts (see Heintz et al. 2023b, for further details).

All the results presented above exploited the best existing samples of GRB hosts, but are strongly impacted by poor statistics due to the small number of events, especially at high-redshift. To date, GRB 130606A (Hartoog et al. 2013) and GRB 210905A (Saccardi et al. 2023), at $z = 5.913$ and $z = 6.312$,

respectively, are the highest redshift GRBs with available optical and NIR spectroscopy of their afterglow characterized by high SNR, good spectral resolution and a large number of detected absorption lines of the neutral gas in their host galaxies. With these afterglow spectra it was possible to study the chemical abundance pattern and depletion of metals, and to retrieve information on nucleosynthesis, all in an unprecedented detail for faint galaxies at such high-redshift (Chornock et al. 2013; Totani et al. 2014; Hartoog et al. 2015; Rossi et al. 2022; Saccardi et al. 2023; Faussey et al. 2025).

In this paper, we study the VLT/X-shooter optical and NIR afterglow spectrum of GRB 240218A at redshift $z = 6.782$. In Sect. §2 and §3, we present our dataset, the fitting of the absorption lines, together with the curve of growth analysis and the GRB-absorbers distance calculation. In Sect. §4 we present our results. Discussion and conclusions are drawn in Sect. §5. A Λ CDM cosmological model with $\Omega_M = 0.308$, $\Omega_\Lambda = 0.692$, and $H_0 = 67.8 \text{ km s}^{-1} \text{ Mpc}^{-1}$ (Planck Collaboration et al. 2016) has been assumed for calculations. All data are in observer frame and 1σ errors are reported throughout the paper, unless otherwise specified. A companion paper (Brivio et al. 2025) presents and analyzes the GRB prompt and afterglow multiwavelength spectral and temporal properties, comparing with those of the few high-redshift LGRBs observed so far and those of lower- z events.

2. VLT/X-shooter observation of GRB 240218A

On February 18, 2024, at 02:00:00 UT the *Neil Gehrels Swift Observatory* (*Swift* hereafter; Gehrels et al. 2004) discovered GRB 240218A. The *Swift* Burst Alert Telescope (BAT, Barthelmy et al. 2005) triggered and located the explosion (Page et al. 2024). *Swift* slewed immediately to the burst and the X-Ray Telescope (XRT, Burrows et al. 2005) began observing the field 149.4 seconds after the BAT trigger. XRT found a bright, uncatalogued X-ray source at the enhanced position of coordinates RA (J2000) = 10h 47m 11.24s Dec. (J2000) = +01° 16′ 34.8″ with an uncertainty of 4.2″ (Evans et al. 2024). The *Swift* Ultra-Violet and Optical Telescope (UVOT, Roming et al. 2005) took a finding chart exposure of 119 seconds with the White filter starting 158 s after the BAT trigger. No credible afterglow candidate was found in the data products. Follow-up from the ground allowed the detection of a bright NIR afterglow candidate (D’Avanzo et al. 2024; Rossi et al. 2024) and its optical counterpart (Malesani 2024), together with a precise localization of the afterglow thanks to the radio (Schroeder et al. 2024; Thakur et al. 2024) and mm (Laskar et al. 2024) detections (see Brivio et al. 2025 for further details).

Table 1: Log of the observations.

Epoch (Hours)	Arm	Exp. time (s)	Wav. range (Å)	Slit (′′)	Resolution R ($\lambda/\delta\lambda$)
26.47	UVB	4x1200	3000-5600	1.0x11	5400
26.47	VIS	4x1200	5600-10200	0.9x11	8900
26.47	NIR	8x600	10200-21000	0.9x11JH	5600

Approximately ~ 26 hr (observer frame) after the detection of GRB 240218A, we observed its afterglow using the ESO VLT UT3 equipped with the X-shooter spectrograph (Vernet et al. 2011). The observing setup is detailed in Table 1. Observations were conducted using the ABBA nod-on-slit mode. Each individual spectrum from the UVB and VIS arms was reduced using the STARE mode reduction, with the extraction window po-

sitioned at the GRB afterglow trace. The NIR arm data were processed using the standard X-shooter NOD mode pipeline (Goldoni et al. 2006; Modigliani et al. 2010). Sky features were subtracted and each flux-calibrated spectrum was combined into a final science spectrum. Additionally, a telluric correction was applied to the final stacked VIS and NIR spectra, and wavelengths were corrected to the vacuum-heliocentric system. To ensure a correct flux calibration between the VIS and NIR arms, both spectra were normalized to the afterglow photometry in the z and J band, respectively, reported at the mean time of the spectrum using the light curve fit provided by Brivio et al. (2025) which presents a complete analysis of the multiwavelength light curve. An integration of the spectrum over the filter profile was necessary given that the H I absorption (Lyman- α break) significantly affects the z -band magnitude.

3. Data analysis

The highest redshift system identified in the absorption spectrum of GRB 240218A afterglow is at $z = 6.782$ and spans $\sim 400 \text{ km s}^{-1}$. It is a DLA absorption system (see Figure 1) with associated metal absorption lines (Saccardi et al. 2024). As this is the highest redshift H I absorption in the spectrum and, furthermore, fine-structure absorption lines are detected corresponding to this system, we associate it with the host galaxy of GRB 240218A. We do not identify any foreground intervening absorbers along the line of sight. We note that this is the highest GRB redshift measured accurately from metal absorption lines so far.

3.1. The damped Ly- α absorption feature

The DLA absorption imprinted from H I in the host-galaxy ISM is shown in Figure 1.

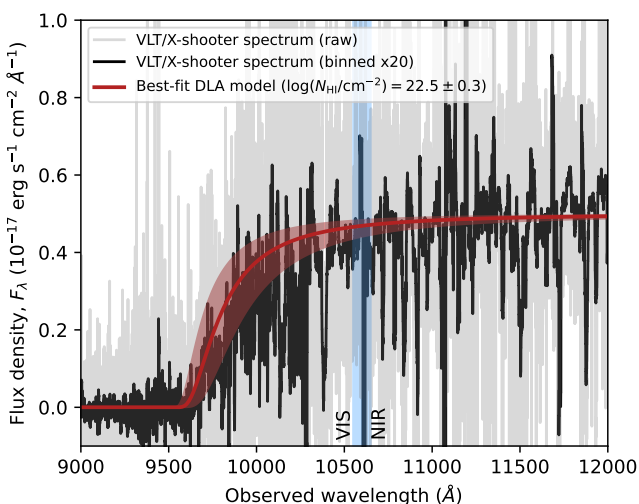


Fig. 1: VLT/X-shooter 1D spectrum of GRB 240218A. The grey curve show the raw, stitched VIS+NIR arm, photometrically calibrated spectrum, and the black the binned version (by a factor of 20). The best-fit DLA model with $\log(N_{\text{HI}}/\text{cm}^{-2}) = 22.5 \pm 0.3$ is shown as the red curve, with the uncertainty represented by the red-shaded area. The connection region between the VIS and NIR arms is represented by the blue-shaded area.

The determination of the DLA column density is complicated by the fact that the red wing falls in a noisy region of the spectrum at the overlap of the VIS and NIR arms. At this high redshift, we also expect a significant neutral H I fraction in the line of sight through the partially neutral IGM.

We model the Ly α damping wing with a Voigt profile, with an optical depth $\tau = CaH(a, x)N_{\text{HI}}$, where C is the photon absorption constant, a is the damping parameter, and $H(a, x)$ is the Voigt-Hjerting function, following the approximation of Tepper-García (2006). We further add the optical depth from the Gunn-Peterson effect from an increasingly neutral intergalactic medium (IGM; Fan et al. 2006), following the approximation by Miralda-Escudé (1998); Totani et al. (2006), integrating the line-of-sight IGM contribution from the GRB redshift down to $z = 6$. We assume that the intrinsic slope can be quantified as a power-law, $F_{\lambda} \propto \lambda^{-\beta}$, and simultaneously constrain the three free parameters in the fit, β , N_{HI} , and x_{HI} . Since the neutral H I fraction of the IGM, x_{HI} , is essentially unconstrained in the modeling due to the substantial local H I component in the GRB host, we fix this quantity to $x_{\text{HI}} = 0.2$ in the final best-fit model. Assuming a single velocity component fixed to the systemic redshift $z_{\text{GRB}} = 6.782$, a final value of $\log(N(\text{H I})/\text{cm}^{-2}) = 22.5 \pm 0.3$ is obtained.

3.2. Metal absorption lines

The low-ions (Fe II, Cr II, Zn II, Si II, Al II, etc.) trace the neutral medium in the host galaxy. In GRB 240218A afterglow spectra, low-ionization lines are detected in three separate components (see Figure 2 and Table 2). Component II is the strongest and shows fine-structure absorption lines; we therefore adopt its redshift ($z_{\text{GRB}} = 6.782$) as that of the GRB host (refer also to analysis in Sect. 4.1 on distance of absorbing gas clouds) and as the zero reference value in velocity space. Components I and III are at $\Delta v = -200 \text{ km s}^{-1}$ and $\Delta v = +50 \text{ km s}^{-1}$, respectively.

For components II and III, the spectrum shows clear detection of transitions arising from excited levels of Fe II, and from metastable levels (involving transitions from long-lived excited states that are forbidden or suppressed by selection rules) of both Fe II and Ni II. The Fe II* $\lambda 2612$, Fe II* $\lambda 1613$, Fe II* $\lambda 1702$ and Ni II* $\lambda 2166$, Ni II* $\lambda 2217$, Ni II* $\lambda 2223$ transitions are identified as shown in Figure 2. A comprehensive analysis of fine-structure absorption lines and cloud distances is presented in Sect. 4.1 and Appendix A.

Despite the very noisy region of the spectrum, high-ionization lines (C IV, Si IV) are also detected, with their strongest component aligned with that of low-ionization transitions. They span a larger range with respect to low-ionization lines in velocity space, $\Delta v \sim 500 \text{ km s}^{-1}$ (see Figure 2).

Most of the low-ionization absorption lines show signs of saturation. The fitting procedure in the saturated regime, flat region of the Curve of Growth (CoG), is not straightforward. Fitting simultaneously multiple transitions of the same ionic element can address the hidden saturation issue. An intermediate-resolution spectrograph, such as X-shooter, can reduce this effect slightly, but caution is needed when interpreting column densities obtained via CoG. Such measurements should generally be considered as lower limits, especially if the equivalent widths (EW s) fall within the saturated region of the CoG (Prochaska 2006). Indeed, at the X-shooter resolution, to get more reliable constraints one should use a combination of the lines with different oscillator strengths. To estimate the column densities of elements with similar ionization potential, we first use the CoG approach, as described in Spitzer (1998) and explained in detail

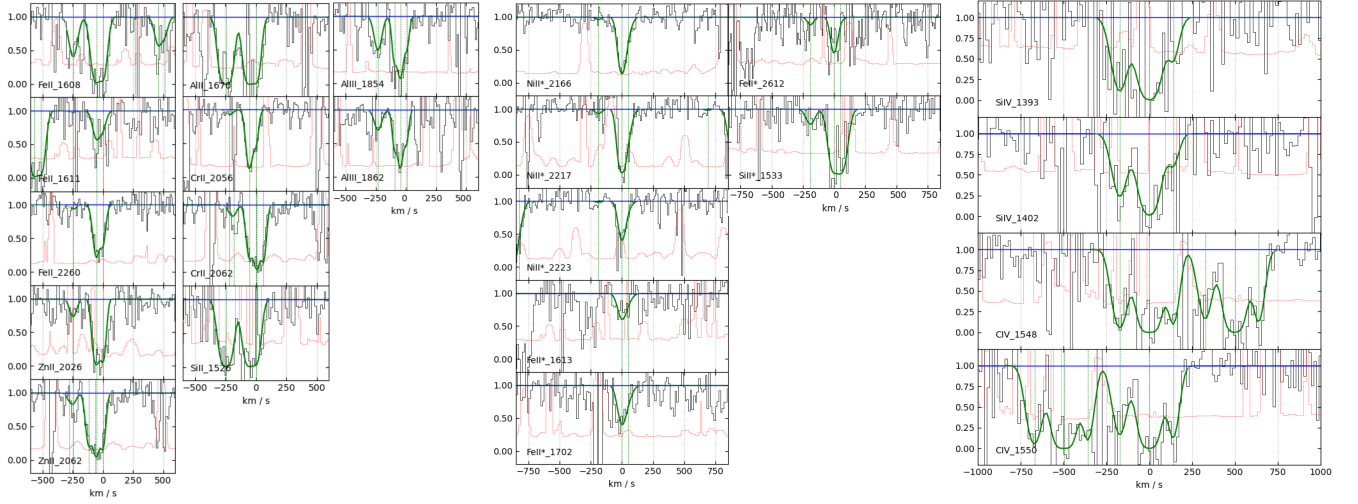


Fig. 2: VLT/X-shooter optical/NIR afterglow spectrum of GRB 240218A. *Left panel*: selection of low-ionization absorption lines of the GRB host galaxy system. Here and in the following panels data are in black, the fit is in green, the error spectrum is in red, the continuum in blue and the vertical green dashed lines indicate the center of the components. *Middle panel*: fine-structure and excited transition absorption lines of the GRB host galaxy system. *Right panel*: high-ionization absorption lines. All the plots are in velocity space and 0 has been fixed to $z = 6.782$ (see Sect. 3), corresponding to the stronger low-ionization line component (II).

Table 2: *Top*: Column density of low-ionization lines. *Bottom*: Column density of high-ionization lines. The last row reports the Doppler parameter b used of each component as resolved by the X-shooter observations. Results assuming column densities as measurements are reported in square brackets.

Species	<i>I</i>	<i>II</i>	<i>III</i>
	-200 km s^{-1}	0 km s^{-1}	$+50 \text{ km s}^{-1}$
Al II $\lambda 1670$	> 14.7	> 15.0	> 14.5
Zn II $\lambda 2026, \lambda 2062$	12.9 ± 0.2	$> 14.1 [14.1 \pm 0.2]$	$> 13.9 [13.9 \pm 0.1]$
Cr II $\lambda 2056, \lambda 2062$	13.0 ± 0.2	$> 14.4 [14.4 \pm 0.1]$	$> 13.8 [13.8 \pm 0.1]$
Si II $\lambda 1526$	> 15.9	> 16.5	> 15.5
Fe II $\lambda 1608, \lambda 1611, \lambda 2260^{\ddagger}$	14.6 ± 0.1	$> 15.8 [15.8 \pm 0.1]$	$> 15.6 [15.6 \pm 0.1]$
Fe II* $\lambda 2612$ (1s)	< 13.3	13.8 ± 0.1	12.6 ± 0.4
Fe II* $\lambda 1613, \lambda 1702$ (5s)		14.5 ± 0.1	13.8 ± 0.3
Si II* $\lambda 1533$	< 12.4	> 14.8	> 15.1
Ni II* $\lambda 2166, \lambda 2217, \lambda 2223$	< 12.9	14.2 ± 0.1	13.3 ± 0.1
Al III $\lambda 1854, \lambda 1862^{\dagger}$	13.3 ± 0.2	> 14.1	> 13.2
$b \text{ (km s}^{-1}\text{)}^*$	34 ± 4	27 ± 4	21 ± 4

Species	1	2	3
	-200 km s^{-1}	0 km s^{-1}	$+140 \text{ km s}^{-1}$
C IV $\lambda 1548, \lambda 1550^{\S}$	> 14.7	> 15.7	> 15.8
Si IV $\lambda 1393, \lambda 1402^{\S}$	> 14.3	> 15.2	> 13.7
$b \text{ (km s}^{-1}\text{)}$	38 ± 4	44 ± 4	17 ± 4

\ddagger Other Fe II transitions are identified in the absorption spectrum e.g. Fe II $\lambda 2344, \lambda 2374, \lambda 2587, \lambda 2600$. Unfortunately, they fall in a region of the spectrum strongly affected by telluric absorption and with poor SNR. For this reason they are not taken into account when performing the Voigt-profile fitting.

\dagger Component II of Al III is fitted with a different Doppler parameter, $b \text{ (km s}^{-1}\text{)} = 47 \pm 4$, due to its different ionization energy.

\S C IV and Si IV lines are particularly uncertain because they are found in a very noisy region of the spectrum.

* The determined b -values are rather high and this probably means that the components are composed of multiple narrower ones.

in Appendix B. The best-fit CoG is illustrated in Figure 3. The results show a quite high Doppler parameter b , likely indicating spectrally unresolved components, and that most of the transitions fall at the knee of the CoG (see Figure 3), which is the transition region between linear and saturated regime.

It is evident that the large EW (see Table B.1) of the metal lines (e.g. Fe II $\lambda 2260$, Zn II doublet) is remarkable at such high redshift. They are not only significantly stronger than what

is typically observed in GRB-DLAs (de Ugarte Postigo et al. 2012), but also comparable to the values commonly observed in the Milky Way (MW; e.g., De Cia et al. 2021).

We then performed a Voigt fit profile analysis to determine the element column densities. This is another approach which follows the same physical method as CoG with the only difference being that the latter, relying on EW measurements, does not depend on spectral resolution. We fit the systems with the *Astro-*

cook code (Cupani et al. 2020), a *Python* software environment to analyze absorption spectra that includes a set of algorithms to model spectral features in absorption and emission (continuum, spectral lines, complex absorption systems). The column densities that we determined are presented in Table 2. The errors reported are those obtained by the line fitting.

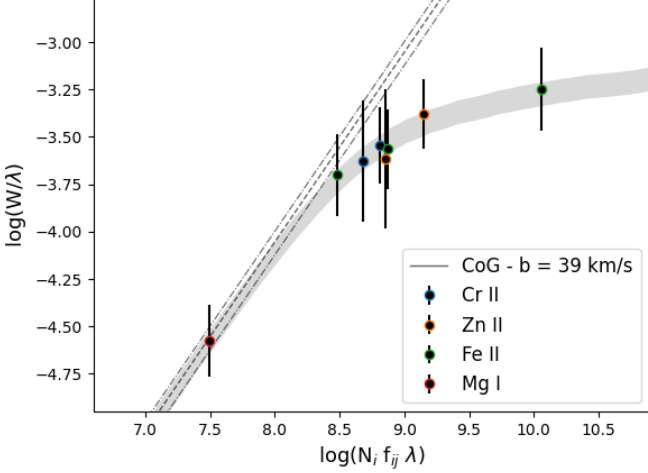


Fig. 3: Results obtained from the CoG analysis on the ISM absorption lines identified in the spectrum of GRB 240218A. The data points are color-coded with respect to different element transitions (see Table B.1). The grey shaded area represents the best fit model which results in the labeled value of the Doppler parameter, while the dotted lines represent the linear approximation regime and its 1σ confidence ranges.

The simultaneous fit of all the transitions of the Cr II multiplet¹ (Cr II $\lambda 2056$, Cr II $\lambda 2062$) makes it possible to estimate the chromium column density. The flux residual of Cr II $\lambda 2056$ suggests that the Cr II column density may be considered as a lower limit. Concerning iron, the Fe II $\lambda 2260$ transition shows as well flux residuals which are at the limit of saturation. The Fe II $\lambda 1611$ transition does not appear to be saturated as shown in Figure 2. It would confirm that the Fe II $\lambda 2260$ transition is not affected by severe saturation. However, given the bad SNR region where the $\lambda 1611$ transition falls, we may also consider the Fe II column density as a lower limit. On the other hand, Zn is a more delicate case. Figure 2 shows evidence for some saturation of Zn II $\lambda 2026$, while the Zn II $\lambda 2062$ is blended with Cr II $\lambda 2062$. By measuring the Cr II column density with the Voigt-profile fitting, it is possible to deblend the lines and recover the contribution of Zn II². As for the other elements it would be cautious to take the Zn II column density as a lower limit to avoid incorrect conclusion and a systematic underestimate of all column density. We note that, with respect to our scientific results (see Sect. 4.2), considering the Zn II column density as a measurement is a conservative approach.

As expected, the Voigt fit approach and the CoG provide consistent results. Indeed, considering a single component even for the Voigt fit profile analysis, the Doppler parameter is in agreement with that determined by the CoG.

¹ The Cr II $\lambda 2066$ transition, which would be the weakest of the triplet (Cr II $\lambda 2056$, Cr II $\lambda 2062$, Cr II $\lambda 2066$) is strongly affected by a sky line.

² The same method has been applied for Zn II $\lambda 2026$ which is blended with Mg I $\lambda 2026$.

4. Results

4.1. Fine-structure lines and absorbing cloud distances

GRB afterglows strongly interact with the interstellar medium, by depositing a large amount of energy. This is particularly evident in the optical-UV band where the gas surrounding the GRB absorbs the radiation, exciting the atoms and ions to high quantum levels. The comparison of observations with predictions from time dependent photo-excitation codes has been applied to the spectra of several GRBs (Dessauges-Zavadsky et al. 2006; D’Elia et al. 2009a; Ledoux et al. 2009; Hartoog et al. 2013; D’Elia et al. 2014; Saccardi et al. 2023; Pugliese et al. 2024), allowing estimates of the distance between the GRB and the absorber, which typically spans tens to hundreds of pc (Vreeswijk et al. 2012).

For GRB 240218A we can apply the comparison between data and photo-excitation codes to find the distance between the GRB and the absorbers of components II and III (we refer to the Appendix A for more details). We find $d_{II} = 620^{+230}_{-140}$ pc, $d_{III} = 2.0^{+7.6}_{-0.6}$ kpc, for component II and III, respectively. Despite the large uncertainties for component III due to the larger errors on the column densities, we can safely conclude that component II lies closer to the GRB than component III. We note that these distances could be larger if the ground state column densities are underestimated (if affected by saturation).

4.2. Metallicity and chemical enrichment of the neutral gas

We used the metal and neutral hydrogen column densities to determine the metallicity of GRB 240218A host galaxy along the GRB line of sight. Based on the column density of Zinc ($\log(N(\text{Zn II})/\text{cm}^{-2}) > 14.3$), that is a poorly dust depleted element, we calculate the observed metallicity $[X/H] > -0.8$ (where X is Zn).

Despite being aware of the limitations of the spectral data, especially regarding the saturation issues, we report here a deeper analysis on the chemical enrichment and dust depletion by assuming column densities of Fe II, Cr II, and Zn II as measurements. We used the metal and neutral hydrogen column densities reported in Table 3, assuming Asplund et al. (2021) solar abundances.

Table 3: Column densities, metal abundances, and relative abundances with respect to iron. Results assuming column densities as measurements are reported in square brackets.

X	$\log(N/\text{cm}^{-2})$	[X/H]	[X/Fe]
Al	> 15.3	> -1.7	$[> 0.3]$
Zn	$> 14.3 [14.3 \pm 0.2]$	$[-0.8 \pm 0.4]$	$[1.2 \pm 0.2]$
Si	> 16.6	> -1.4	$[> 0.6]$
Fe	$> 16.0 [16.0 \pm 0.1]$	$[-1.9 \pm 0.3]$	
Cr	$> 14.5 [14.5 \pm 0.1]$	$[-1.6 \pm 0.3]$	$[0.3 \pm 0.1]$

Following the method developed by De Cia et al. (2016), De Cia et al. (2021) (but using the most recent and solid compilation of the so-called refractory indices from Konstantopoulou et al. 2024), we analyze the abundances of different metals with the aim of characterizing the chemical enrichment in the GRB host galaxy. We stress that this deeper analysis on the chemical enrichment and dust depletion is based on the assumption of considering, despite the possible saturation issue, the column densities values as measures and not as limits.

Despite the large uncertainties and the limited amount of elements available, the abundance pattern shown in Figure 4 indicates clearly significant dust depletion. We fit a linear relation³ to the constrained data (Cr, Fe, and Zn), and not including Al and Si⁴.

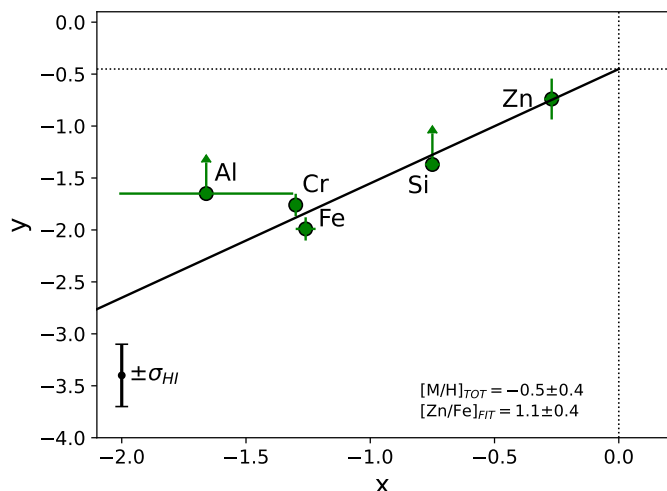


Fig. 4: Abundance pattern observed in the host of GRB 240218A from the total absorption-line profile. The observed abundances are on the y-axis, and the x-axis represent the tendency of each element to deplete into dust grains. The linear fit to the data (solid line) determines the dust depletion corrected metallicity $[M/H]_{\text{tot}}$ (intercept) and the overall strength of depletion $[Zn/Fe]_{\text{fit}}$ (slope). The H I error bar, the same for all the data points, is reported as σ_{HI} . See De Cia et al. (2021, 2024) and Konstantopoulou et al. (2024) for a exhaustive description of the method.

The dust-corrected metallicity is $[M/H]_{\text{tot}} = -0.5 \pm 0.4$ with a dust depletion of $[Zn/Fe]_{\text{fit}} = 1.1 \pm 0.4$. The large uncertainties are mainly due to the low SNR of the X-shooter spectrum. We note that considering Zn II column density as a lower limit would imply even higher metallicity and dust depletion values.

Following Konstantopoulou et al. (2024) we derive the dust-to-metal mass ratio (DTM), that is the ratio between the mass of dust and the total mass of the metals. We find $DTM = 0.5 \pm 0.1$. This DTM value, together with that of $[Zn/Fe]_{\text{fit}}$, is similar to what is observed in the MW. The GRB-selected galaxies further show systematically lower DTM than the MW, especially at high-redshift (Heintz et al. 2023b). Hence, GRB 240218A DTM value represents an exception with respect to the best-fit relation derived from observed GRB-DLA (Heintz et al. 2023b) and values predicted by the simulations (Li et al. 2019).

The above results bring to a high value of $A_{V,\text{depl}} \sim 5$. The uncertainty on the extinction value derived from depletion ($A_{V,\text{depl}}$) is also high due to the large uncertainties on the total dust-corrected metallicity and H I column density, and it is not possi-

³ For more details on the method please refer to De Cia et al. (2024) (i.e. in particular to Figure 3) and Konstantopoulou et al. (2024); see also Saccardi et al. (2023) for a direct application of such a method to the high-redshift case of GRB 210905A.

⁴ In previous high redshift GRB-DLAs there is the evidence of an Al overabundance (see Sect. 4). Its deviation from the linear fit is much more related to nucleosynthesis effect rather than dust depletion. Hence, its inclusion in the fit could bias the results. We also exclude Si from the linear fit for the same reasons (nucleosynthesis). We thus consider them as lower limits and not taking into account during the fit procedure.

ble to place an accurate constraint on this measure. The amount of extinction needed to reproduce the afterglow spectral energy distribution (SED) is $A_{V,\text{SED}} = 0.35 \pm 0.03$ mag (Brivio et al. 2025).

Notably, we observe a sign of aluminium overabundance (see Figure 4, and Appendix C). This is also the case in the other two high- z GRB afterglows with a comprehensive analysis of the abundance patterns, GRB 130606A (Hartoog et al. 2015) at $z = 5.913$ and GRB 210905A (Saccardi et al. 2023) at $z = 6.312$. This peculiar chemical pattern, nowadays found typically in globular clusters, can be the direct signature of the presence of very massive rotating stars (Prantzos et al. 2007, and references therein). Furthermore, we perform a component-by-component analysis of the depletion patterns. All show a strong amount of dust depletion, and component I shows a clear evidence of aluminum overabundance. The details of this analysis are shown in Appendix C. In Figures C.2 and C.3 we show the linear fit for each component and the over- and under-abundance of the different elements with respect to iron after correcting for dust depletion, respectively.

5. Discussion and conclusions

We analyzed the gas properties along the GRB 240218A line of sight using afterglow spectra obtained with VLT/X-shooter. Our study reveals the presence of neutral hydrogen, low-ionization, high-ionization, and fine-structure metal lines, originating from the GRB host galaxy complex at $z = 6.782$. We measured a high neutral hydrogen column density in the host galaxy of $\log(N(\text{H I})/\text{cm}^{-2}) = 22.5 \pm 0.3$. We determined the abundances of metals in the neutral gas of the ISM along the GRB line of sight ($[Zn/H] > -0.8$). Under the assumption that the column densities can be derived although aware of the saturation issue, we found evidences of high dust depletion, that we estimate to correspond to $[Zn/Fe]_{\text{fit}} = 1.1 \pm 0.4$, resulting in a dust-corrected metallicity of $[M/H]_{\text{tot}} = -0.5 \pm 0.4$.

The host galaxy of GRB 240218A has the highest neutral hydrogen column density measured at high-redshift ($z \gtrsim 6$) for any GRB sight-line detected thus far. The large H I column density indicates that the host galaxy contains and/or is surrounded by massive, extended clouds of neutral gas, which is the raw material for star formation in galaxies. Intriguingly, such high $\log(N(\text{H I}))$ have been reported also by Heintz et al. (2024) for three DLAs at $z > 8$ observed with JWST (see Figure 5), and are now also detected in very high-redshift galaxies (e.g. Hainline et al. 2024; Witstok et al. 2025).

Furthermore, the large amount of metals (and likely dust) already formed at high-redshift is surprising compared to previous studies or high- z simulation (Heintz et al. 2023b; Li et al. 2019). This is the first time that strong absorption lines of metals, such as those of Zn II, have been observed at high redshift. We investigated the extent to which the high column densities measured for Zn II and Cr II in the ISM of this host galaxy is likely due to the large amounts of dense gas, as suggested by the large amount of neutral hydrogen. Hence, we compared our column density measurements with those of other GRBs for which these quantities are available. We first selected GRBs for which $\log(N(\text{H I})/\text{cm}^{-2}) > 22$ has been measured in Tanvir et al. (2019), supplemented by more recent results. Within the selected GRBs, we then looked for the ones that had Zn and Cr column density measurements available. This led to the construction of the

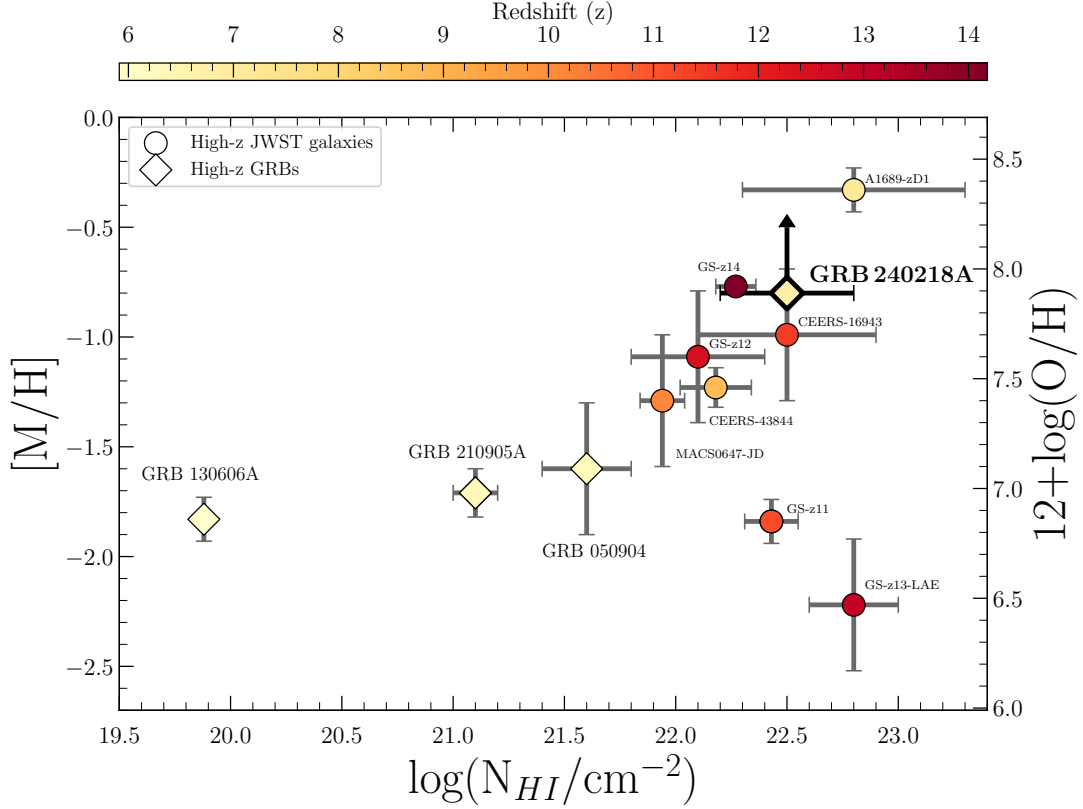


Fig. 5: Metallicity as a function of $\log(N_{\text{HI}}/\text{cm}^{-2})$ color-coded by the redshift for GRBs host galaxies and high-redshift galaxies observed with JWST. For GRBs hosts, we report the observed metallicity ($[M/H]$, not corrected for dust-depletion) determined from the afterglow spectra of GRBs at $z \geq 6$, i.e. GRB 050904 (Kawai et al. 2006; Thöne et al. 2013; note that the measurements rely on a low-resolution spectrum), GRB 130606A (Hartoog et al. 2015; Heintz et al. 2023b), GRB 210905A (Saccardi et al. 2023). For high-redshift galaxies, we report the oxygen based metallicity determined from emission lines and/or SED fitting for the recently discovered JWST high-redshift galaxies, i.e. GS-z14 (Carniani et al. 2025; Heintz et al. 2025), GS-z12 (D’Eugenio et al. 2024), GS-z11 (Hainline et al. 2024), GS-z13-LAE (Witstok et al. 2025), CEERS-43844, MACS0647-JD, CEERS-16943 (Heintz et al. 2024), A1689-zD1 (Watson et al. 2015; Heintz et al. in prep). The relationship between $12+\log(\text{O}/\text{H})$ and $[M/H]$ is defined by the comparison with the solar oxygen abundance, where $[M/H] = 12+\log(\text{O}/\text{H}) - 8.69$ (Asplund et al. 2021).

sample⁵ reported in Figure 6. Certainly, as already stressed, the column density of Zn II, but also of Cr II, is an exception at high redshift. Furthermore, it also turns out to be an exception in comparison with low-redshift analogs. Indeed, from Figure 6 it is clear that these large column densities are less common at low-redshift.

In summary, GRB 240218A host galaxy is very likely a massive high-redshift galaxy, characterized by a large amounts of neutral gas, neutral hydrogen column and metals showing substantial, rapid chemical evolution and enrichment, as indicated by the significant presence of metals (and likely dust). Such properties could imply the need for sustained star formation before the GRB to build up the metals. The GRB is thus likely hosted by a massive galaxy that formed early. This GRB host galaxy is very extreme among GRB- and QSO-DLAs, which trace a common population of (low-mass) galaxies at intermediate redshifts. On the other hand, this substantial enrichment of metals and dust of the ISM is in agreement with recent findings (see Figure 5) based on strong nebular emission lines of star-forming regions of high-redshift galaxies at $z \sim 7$ observed with

JWST (Langeroodi et al. 2023; Heintz et al. 2023a; Nakajima et al. 2023; Curti et al. 2024; Roberts-Borsani et al. 2024; Heintz et al. 2025), as well as with the metal and dust rich high- z quasars host galaxies (Triptodi et al. 2023, 2024; Salvestrini et al. 2025). The fact that such properties are found in GRB host galaxies is particularly interesting because, at high-redshift, these galaxies are selected based only on being star-forming.

While JWST usually allows the study of the metallicity of the ionized gas, the explosion of GRB 240218A has allowed a detailed chemical analysis of the neutral ISM of a high-redshift galaxy. These are unprecedented measurements for a galaxy at $z \sim 7$. Another advantage of GRB host galaxy studies is that, in addition to the neutral gas absorption feature, it is possible to observe the continuum and emission lines of the host galaxy, once the GRB afterglow faded. Photometric and spectroscopic observations of the host galaxy of GRB 240218A with ALMA and JWST would provide a unique opportunity to integrate the chemical properties and the kinematics of the neutral gas studied in this work with those of the ionized gas (e.g. Schady et al. 2024), and add unprecedented details on the chemical and physical properties of high-redshift galaxies. In this sense, it will also be possible to compare these future results with other GRB host galaxies at high-redshift by starting to construct a useful sample.

⁵ GRB 050401; GRB 111008A; GRB 120119A; GRB 120327A; GRB 120716A; GRB 120815A; GRB 140311A; GRB 141109A; GRB 151021A; GRB 180325A; GRB 181020A; GRB 190114A

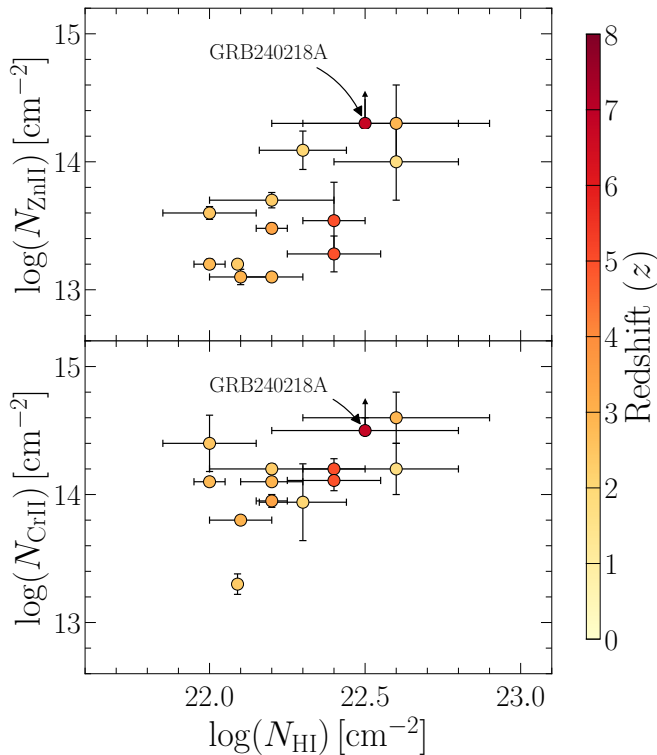


Fig. 6: Column density of Zn II (Watson et al. 2006; Wiseman et al. 2017; Heintz et al. 2019; Bolmer et al. 2019; Selsing et al. 2019) versus $\log(N(\text{H I})/\text{cm}^{-2})$ (Tanvir et al. 2019), color-coded by the GRB host galaxy redshift. GRB 240218A is marked and compared with the sample of GRBs for which these measurements are available.

Our results emphasize that ground-based spectroscopic observations of absorption lines in the spectra of bright background sources, such as GRBs, are powerful tools to explore the chemical properties of the neutral gas in distant galaxies. It has been shown (e.g. Ghirlanda et al. 2015) that, to efficiently detect the prompt emission from high-redshift GRBs (that is the necessary first step to trigger the afterglow observations), it is essential to extend the energy range of space satellite detectors of the prompt emission to lower energies (e.g. SVOM, launched in June 2024, Wei et al. 2016; *Einstein Probe*, Yuan et al. 2015, 2022), and to improve sensitivity to lower flux detection limits (e.g. THE-SEUS, selected for ESA M7 Phase-A, Amati et al. 2018; Tanvir et al. 2021). We stress also that the localization capabilities of mission with such characteristics is fundamental to enhance the possibility of optical/NIR spectroscopic observations with high SNR of GRBs afterglows. Furthermore, high-resolution absorption spectroscopy of the X-ray afterglow by the ESA large mission *NewAthena* can extend our knowledge of the metal abundances much closer to the GRB, thus providing a powerful diagnostics of the GRB progenitors in the high-redshift Universe (Piro et al. 2022).

The results of our study of GRB 240218A motivate pursuing GRB-dedicated space missions to fully exploit the possibility to use GRBs to explore the high-redshift Universe, in synergy with forthcoming ground-based instruments like the Son Of X-Shooter (SOXS, Schipani et al. 2018), and new facilities such as the future European Southern Observatory (ESO)/Extremely Large Telescope (ELT) equipped with the ArmazoNes high Dispersion Echelle Spectrograph (ANDES) high-resolution spectro-

graph (Marconi et al. 2024; D’Odorico et al. 2024). Furthermore, a novel approach to the discovery of high-redshift GRBs such as the High-z Universe GRB Observatory (HUGO, Campana et al. 2022) will complement the above efforts, taking advantage of the deep monitoring of the sky by the Vera Rubin Observatory (Ivezić et al. 2019), to simultaneously observe exactly the same fields with a dedicated NIR facility.

Acknowledgements. A.S. acknowledges support by a postdoctoral fellowship from the CNES. S.D.V. acknowledges the support of the French Agence Nationale de la Recherche (ANR), under grant ANR-23-CE31-0011 (project PE-GaSus). L.I. acknowledges financial support from the INAF Data Grant Program “YES” (PI: Izzo) Multi-wavelength and multi messenger analysis of relativistic supernovae. This work has received funding from the Swiss State Secretariat for Education, Research and Innovation (SERI) under contract number MB22.00072. The Cosmic Dawn Center (DAWN) is funded by the Danish National Research Foundation under grant DNRF140. NRT acknowledges support from STFC Consolidated Grant ST/W00857/1. R.B. acknowledges funding from the Italian Space Agency, contract ASI/INAF n. 1/004/11/6.

References

- Amati, L., O’Brien, P., Götz, D., et al. 2018, *Advances in Space Research*, 62, 191
- Asplund, M., Amarsi, A. M., & Grevesse, N. 2021, *A&A*, 653, A141
- Barthelmy, S. D., Barbier, L. M., Cummings, J. R., et al. 2005, *Space Sci. Rev.*, 120, 143
- Bolmer, J., Ledoux, C., Wiseman, P., et al. 2019, *A&A*, 623, A43
- Brivio, R., Campana, S., Covino, S., et al. 2025, *A&A*, 695, A239
- Bunker, A. J., Saxena, A., Cameron, A. J., et al. 2023, *A&A*, 677, A88
- Burrows, D. N., Hill, J. E., Nousek, J. A., et al. 2005, *Space Sci. Rev.*, 120, 165
- Campana, S., Ghirlanda, G., Salvaterra, R., et al. 2022, *Nature Astronomy*, 6, 1101
- Cano, Z., Wang, S.-Q., Dai, Z.-G., & Wu, X.-F. 2017, *Advances in Astronomy*, 2017, 8929054
- Carniani, S., D’Eugenio, F., Ji, X., et al. 2025, *A&A*, 696, A87
- Castellano, M., Napolitano, L., Fontana, A., et al. 2024, *ApJ*, 972, 143
- Chornock, R., Berger, E., Fox, D. B., et al. 2013, *ApJ*, 774, 26
- Cucchiara, A., Levan, A. J., Fox, D. B., et al. 2011, *ApJ*, 736, 7
- Cupani, G., D’Odorico, V., Cristiani, S., et al. 2020, in *Society of Photo-Optical Instrumentation Engineers (SPIE) Conference Series*, Vol. 11452, Society of Photo-Optical Instrumentation Engineers (SPIE) Conference Series, 114521U
- Curti, M., Maiolino, R., Curtis-Lake, E., et al. 2024, *A&A*, 684, A75
- Curti, M., Wistok, J., Jakobsen, P., et al. 2025, *A&A*, 697, A89
- D’Avanzo, P., Ferro, M., Brivio, R., et al. 2024, *GRB Coordinates Network*, 35747, 1
- De Cia, A., Jenkins, E. B., Fox, A. J., et al. 2021, *Nature*, 597, 206
- De Cia, A., Ledoux, C., Mattsson, L., et al. 2016, *A&A*, 596, A97
- De Cia, A., Ledoux, C., Petitjean, P., & Savaglio, S. 2018, *A&A*, 611, A76
- De Cia, A., Ledoux, C., Savaglio, S., Schady, P., & Vreeswijk, P. M. 2013, *A&A*, 560, A88
- De Cia, A., Roman-Duval, J., Konstantopoulou, C., et al. 2024, *A&A*, 683, A216
- de Ugarte Postigo, A., Fynbo, J. P. U., Thöne, C. C., et al. 2012, *A&A*, 548, A11
- de Wet, S., Izzo, L., Groot, P. J., et al. 2023, *A&A*, 677, A32
- D’Elia, V., Campana, S., Covino, S., et al. 2011, *MNRAS*, 418, 680
- D’Elia, V., Fiore, F., Perna, R., et al. 2009a, *ApJ*, 694, 332
- D’Elia, V., Fiore, F., Perna, R., et al. 2009b, *A&A*, 503, 437
- D’Elia, V., Fynbo, J. P. U., Covino, S., et al. 2010, *A&A*, 523, A36
- D’Elia, V., Fynbo, J. P. U., Goldoni, P., et al. 2014, *A&A*, 564, A38
- Dessauges-Zavadsky, M., Prochaska, J. X., D’Odorico, S., Calura, F., & Matteucci, F. 2006, *A&A*, 445, 93
- D’Eugenio, F., Maiolino, R., Carniani, S., et al. 2024, *A&A*, 689, A152
- D’Odorico, V., Bolton, J. S., Christensen, L., et al. 2024, *Experimental Astronomy*, 58, 21
- Evans, P. A., Goad, M. R., Osborne, J. P., Beardmore, A. P., & Swift-XRT Team. 2024, *GRB Coordinates Network*, 36166, 1
- Fan, X., Carilli, C. L., & Keating, B. 2006, *ARA&A*, 44, A15
- Faussey, H. M., Vejlgaard, S., van der Horst, A. J., et al. 2025, *MNRAS*, 536, 2839
- Foreman-Mackey, D., Hogg, D. W., Lang, D., & Goodman, J. 2013, *PASP*, 125, 306
- Fruchter, A. S., Levan, A. J., Strolger, L., et al. 2006, *Nature*, 441, 463
- Gehrels, N., Chincarini, G., Giommi, P., et al. 2004, *ApJ*, 611, 1005
- Gehrels, N. & Razzaque, S. 2013, *Frontiers of Physics*, 8, 661
- Ghirlanda, G., Salvaterra, R., Ghisellini, G., et al. 2015, *MNRAS*, 448, 2514

- Goldoni, P., Royer, F., François, P., et al. 2006, in *Society of Photo-Optical Instrumentation Engineers (SPIE) Conference Series*, Vol. 6269
- Hainline, K. N., D'Eugenio, F., Jakobsen, P., et al. 2024, *ApJ*, 976, 160
- Hartoog, O. E., Malesani, D., Fynbo, J. P. U., et al. 2015, *A&A*, 580, A139
- Hartoog, O. E., Wiersema, K., Vreeswijk, P. M., et al. 2013, *MNRAS*, 430, 2739
- Heintz, K. E., Bolmer, J., Ledoux, C., et al. 2019, *A&A*, 629, A131
- Heintz, K. E., Brammer, G. B., Giménez-Arteaga, C., et al. 2023a, *Nature Astronomy*, 7, 1517
- Heintz, K. E., Brammer, G. B., Watson, D., et al. 2025, *A&A*, 693, A60
- Heintz, K. E., De Cia, A., Thöne, C. C., et al. 2023b, *A&A*, 679, A91
- Heintz, K. E., Watson, D., Brammer, G., et al. 2024, *Science*, 384, 890
- Hjorth, J., Malesani, D., Jakobsson, P., et al. 2012, *ApJ*, 756, 187
- Hjorth, J., Sollerman, J., Møller, P., et al. 2003, *Nature*, 423, 847
- Ivezić, Ž., Kahn, S. M., Tyson, J. A., et al. 2019, *ApJ*, 873, 111
- Kann, D. A., White, N. E., Ghirlanda, G., et al. 2024, *A&A*, 686, A56
- Kawai, N., Kosugi, G., Aoki, K., et al. 2006, *Nature*, 440, 184
- Konstantopoulou, C., De Cia, A., Ledoux, C., et al. 2024, *A&A*, 681, A64
- Krogager, J. K., De Cia, A., Heintz, K. E., et al. 2024, *MNRAS*, 535, 561
- Langeroodi, D., Hjorth, J., Chen, W., et al. 2023, *ApJ*, 957, 39
- Laskar, T., Peña, C., Schroeder, G., & Alexander, K. D. 2024, *GRB Coordinates Network*, 35878, 1
- Ledoux, C., Vreeswijk, P. M., Smette, A., et al. 2009, *A&A*, 506, 661
- Li, Q., Narayanan, D., & Davé, R. 2019, *MNRAS*, 490, 1425
- Madau, P. & Dickinson, M. 2014, *ARA&A*, 52, 415
- Malesani, D. B. 2024, *GRB Coordinates Network*, 35749, 1
- Marconi, A., Abreu, M., Adibekyan, V., et al. 2024, in *Society of Photo-Optical Instrumentation Engineers (SPIE) Conference Series*, Vol. 13096, Ground-based and Airborne Instrumentation for Astronomy X, ed. J. J. Bryant, K. Motohara, & J. R. D. Vernet, 1309613
- Miralda-Escudé, J. 1998, *ApJ*, 501, 15
- Modigliani, A., Goldoni, P., Royer, F., et al. 2010, in *Proc. SPIE*, Vol. 7737, *Observatory Operations: Strategies, Processes, and Systems III*, 773728
- Nakajima, K., Ouchi, M., Isobe, Y., et al. 2023, *ApJS*, 269, 33
- Page, K. L., Parsotan, T. M., Siegel, M. H., & Neil Gehrels Swift Observatory Team. 2024, *GRB Coordinates Network*, 35742, 1
- Péroux, C. & Howk, J. C. 2020, *ARA&A*, 58, 363
- Piro, L., Ahlers, M., Coleiro, A., et al. 2022, *Experimental Astronomy*, 54, 23
- Planck Collaboration, Ade, P. A. R., Aghanim, N., et al. 2016, *A&A*, 594, A13
- Prantzos, N., Charbonnel, C., & Iliadis, C. 2007, *A&A*, 470, 179
- Prochaska, J. X. 2006, *ApJ*, 650, 272
- Prochaska, J. X., Chen, H.-W., & Bloom, J. S. 2006, *ApJ*, 648, 95
- Prochaska, J. X., Dessauges-Zavadsky, M., Ramirez-Ruiz, E., & Chen, H.-W. 2008, *ApJ*, 685, 344
- Pugliese, G., Saccardi, A., D'Elia, V., et al. 2024, *A&A*, 690, A35
- Ramburuth-Hurt, T., De Cia, A., Krogager, J. K., et al. 2023, *A&A*, 672, A68
- Roberts-Borsani, G., Treu, T., Shapley, A., et al. 2024, *ApJ*, 976, 193
- Roming, P. W. A., Kennedy, T. E., Mason, K. O., et al. 2005, *Space Sci. Rev.*, 120, 95
- Rossi, A., Frederiks, D. D., Kann, D. A., et al. 2022, *A&A*, 665, A125
- Rossi, A., Maiorano, E., Stratta, G., D'Avanzo, P., & CIBO Collaboration. 2024, *GRB Coordinates Network*, 35762, 1
- Saccardi, A., Malesani, D. B., Palmerio, J. T., et al. 2024, *GRB Coordinates Network*, 35756, 1
- Saccardi, A., Vergani, S. D., De Cia, A., et al. 2023, *A&A*, 671, A84
- Salvaterra, R., Della Valle, M., Campana, S., et al. 2009, *Nature*, 461, 1258
- Salvestrini, F., Feruglio, C., Tripodi, R., et al. 2025, *A&A*, 695, A23
- Schady, P., Yates, R. M., Christensen, L., et al. 2024, *MNRAS*, 529, 2807
- Schipani, P., Campana, S., Claudi, R., et al. 2018, in *Society of Photo-Optical Instrumentation Engineers (SPIE) Conference Series*, Vol. 10702, Ground-based and Airborne Instrumentation for Astronomy VII, ed. C. J. Evans, L. Simard, & H. Takami, 107020F
- Schroeder, G., Peña, C., Laskar, T., & Alexander, K. D. 2024, *GRB Coordinates Network*, 35794, 1
- Selsing, J., Malesani, D., Goldoni, P., et al. 2019, *A&A*, 623, A92
- Sparre, M., Hartoog, O. E., Krühler, T., et al. 2014, *ApJ*, 785, 150
- Spitzer, L. 1998, *Physical Processes in the Interstellar Medium*
- Tanvir, N. R., Fox, D. B., Levan, A. J., et al. 2009, *Nature*, 461, 1254
- Tanvir, N. R., Fynbo, J. P. U., de Ugarte Postigo, A., et al. 2019, *MNRAS*, 483, 5380
- Tanvir, N. R., Le Floc'h, E., Christensen, L., et al. 2021, *Experimental Astronomy*, 52, 219
- Tepper-García, T. 2006, *MNRAS*, 369, 2025
- Thakur, A. L., Ricci, R., Bruni, G., et al. 2024, *GRB Coordinates Network*, 35866, 1
- Thöne, C. C., Fynbo, J. P. U., Goldoni, P., et al. 2013, *MNRAS*, 428, 3590
- Totani, T., Aoki, K., Hattori, T., et al. 2014, *PASJ*, 66, 63
- Totani, T., Kawai, N., Kosugi, G., et al. 2006, *PASJ*, 58, 485
- Tripodi, R., Feruglio, C., Fiore, F., et al. 2024, *A&A*, 689, A220
- Tripodi, R., Feruglio, C., Kemper, F., et al. 2023, *ApJ*, 946, L45
- Umeda, H., Ouchi, M., Nakajima, K., et al. 2024, *ApJ*, 971, 124
- Vernet, J., Dekker, H., D'Odorico, S., et al. 2011, *A&A*, 536, A105
- Vreeswijk, P. M., Ledoux, C., De Cia, A., & Smette, A. 2012, *Memorie della Societa Astronomica Italiana Supplementi*, 21, 14
- Vreeswijk, P. M., Ledoux, C., Raassen, A. J. J., et al. 2013, *A&A*, 549, A22
- Vreeswijk, P. M., Ledoux, C., Smette, A., et al. 2007, *A&A*, 468, 83
- Watson, D., Christensen, L., Knudsen, K. K., et al. 2015, *Nature*, 519, 327
- Watson, D., Fynbo, J. P. U., Ledoux, C., et al. 2006, *ApJ*, 652, 1011
- Wei, J., Cordier, B., Antier, S., et al. 2016, *ArXiv:1610.06892* [arXiv:1610.06892]
- Wiseman, P., Perley, D. A., Schady, P., et al. 2017, *A&A*, 607, A107
- Witstok, J., Jakobsen, P., Maiolino, R., et al. 2025, *Nature*, 639, 897
- Woosley, S. E. & Bloom, J. S. 2006, *ARA&A*, 44, 507
- Yates, R. M., Péroux, C., & Nelson, D. 2021, *MNRAS*, 508, 3535
- Yuan, W., Zhang, C., Chen, Y., & Ling, Z. 2022, in *Handbook of X-ray and Gamma-ray Astrophysics*, ed. C. Bambi & A. Sanganello, 86
- Yuan, W., Zhang, C., Feng, H., et al. 2015, *arXiv e-prints*, arXiv:1506.07735

¹ Université Paris-Saclay, Université Paris Cité, CEA, CNRS, AIM, 91191, Gif-sur-Yvette, France

² LUX, Observatoire de Paris, Université PSL, CNRS, Sorbonne Université, 92190 Meudon, France

³ Institut d'Astrophysique de Paris, UMR 7095, CNRS-SU, 98 bis boulevard Arago, 75014, Paris, France

⁴ INAF - Osservatorio Astronomico di Capodimonte, Salita Moiarriello 16, 80131, Napoli, Italy

⁵ Niels Bohr Institute, University of Copenhagen, Jagtvej 128, 2200, Copenhagen, Denmark

⁶ Space Science Data Center (SSDC) - Agenzia Spaziale Italiana (ASI), I-00133 Roma, Italy

⁷ Cosmic Dawn Center (DAWN), Denmark

⁸ Department of Astronomy, University of Geneva, Chemin Pegasi 51, 1290 Versoix, Switzerland

⁹ European Southern Observatory, Karl-Schwarzschild Str. 2, 85748 Garching bei München, Germany

¹⁰ Department of Astrophysics/IMAPP, Radboud University, 6525 AJ Nijmegen, The Netherlands

¹¹ Department of physics, University of Calabria, Via P. Bucci, Arcavacata di Rende (CS), Italy

¹² INAF – Osservatorio di Astrofisica e Scienza dello Spazio, Via Piero Gobetti 93/3, 40129 Bologna, Italy

¹³ INFN – Laboratori Nazionali di Frascati, Frascati, Italy

¹⁴ School of Physics and Astronomy, University of Leicester, University Road, Leicester LE1 7RH, UK

¹⁵ INAF – IASF Milano, Via A. Corti 12, 20133 Milano, Italy

¹⁶ Osservatorio Astronomico di Brera, via E. Bianchi 46, I23807, Merate (LC), Italy

¹⁷ Department of Physics & Astronomy, Clemson University, Clemson, SC 29634, USA

¹⁸ University of Warwick, Coventry, CV4 7AL, UK

¹⁹ School of Physics and Centre for Space Research, University College Dublin, Belfield D04 V1W8, Dublin, Ireland

²⁰ INAF - Osservatorio Astronomico di Roma, via Frascati 33, 00040 Monte Porzio Catone, Italy

²¹ Istituto di Astrofisica e Planetologia Spaziali, Via Fosso del Cavaliere 100, 00133 Roma, Italy

²² Astronomical Institute Anton Pannekoek, University of Amsterdam, 1090 GE Amsterdam, The Netherlands

²³ Department of Physics, University of Bath, Bath, BA2 7AY, UK

²⁴ Aix Marseille Université, CNRS, CNES, LAM, Marseille, France

Appendix A: UV pumping and photoionization model

Absorption lines arising from metastable levels were already detected in other GRB afterglow spectra, e.g. Fe II*, Ni II* (Vreeswijk et al. 2007; D’Elia et al. 2009b, 2010, 2011, 2014). As fine-structure lines, the population of the corresponding levels has been shown to be due to the UV radiation (Vreeswijk et al. 2007; D’Elia et al. 2009b). Together with fine-structure lines, excited absorption features produced by metastable levels are used to determine the distance of the closest gas clouds from the GRB responsible for the UV/optical absorption lines (Vreeswijk et al. 2007; Prochaska et al. 2008; D’Elia et al. 2009b; Vreeswijk et al. 2012, 2013). Since the lifetime of high quantum levels state is short, during the spontaneous decay process lower levels are populated, either with principal quantum number $n > 1$ (excited states), or with $n = 1$ but high values of the spin-orbit coupling (the so-called fine-structure levels of the ground state). This process is known as indirect UV pumping and is opposed to the other mechanism able to populate higher levels of the ions and atoms: the collisional processes. The evidence of UV pumping as the primary factor responsible for the population of fine-structure/metastable levels this excitation comes from the variability of the fine-structure levels, which has been reported every time multi-epoch spectroscopy was available (e.g. Prochaska et al. 2006; Vreeswijk et al. 2007; D’Elia et al. 2009a).

For GRB 240218A we have (see Table 2) the detection of the Fe II ground state, the first fine-structure level (marked as 1s), and the ground state of the $n = 2$ first excited state (marked as 5s). These levels have been detected both for component II and III. Instead, no absorption lines are detected at the wavelength corresponding to the ground state of the metastable transitions of Ni II. The low SNR and the strong atmospheric absorption in the region of the spectrum where the Ni II multiplets (Ni II λ 1317, Ni II λ 1370, Ni II λ 1454 and Ni II λ 1709, Ni II λ 1741, Ni II λ 1751) fall, prevent us from determining how much Ni II is in the ground state compared to the excited levels. The scenario in which the Ni II ground state is absent and the Ni II is all in the excited states could be explained by the fact that it takes a long time for the ion to decay to the Ni II ground state, ~ 37 h (Vreeswijk et al. 2007). Hence, transitions from Ni II, and also Fe II, metastable levels serve as strong indicators of the UV pumping mechanism, as they can be detected several hours post-GRB event. Unfortunately, we do not have multi-epoch spectroscopy. However, we note that the Fe II first excited state (5s) has a column density higher than that of the fine structure levels (Table 2). Since collisional processes populate levels according to a Boltzmann distribution, with the lower energy levels being the most populated, this inversion of the population can be interpreted as another signature of the UV pumping mechanism.

The input of the code is the initial column density of the Fe II, which is assumed to be completely in the ground state before it is hit by the GRB afterglow and the Doppler parameter of the absorbing gas. These data have been taken from Table 2 (for the initial column density we summed the columns of the three Fe II levels). We stress that the estimated distances derived from the photoionization model could be larger if the possible saturation issue is not negligible.

Appendix B: Curve of growth analysis

The CoG (for an exhaustive description of the method please refer to eq. 3-50, 3-51 of Spitzer 1998) can be segmented into three smoothly connected regimes, each illustrating a distinct relationship between EW and N : at low EW values ($< 0.1\text{\AA}$), EW is linearly correlated with column density. For intermediate values, the correlation becomes logarithmic ($EW \propto \log(\tau) \propto N_i/b$), and at high values, we observe $EW \propto \sqrt{\tau}$. In the latter two regimes, absorption lines are affected by saturation, making precise N_i estimation challenging, as small EW variations correspond to large N_i changes. This issue can be mitigated by measuring multiple lines from the same transition, particularly if they originate from the ground state to the first excited level, where ions have similar excitation energies and share a common kinetic distribution. A limitation of this method, however, is the lack of detailed velocity distribution information for the multiple ISM clouds contributing to the observed absorption lines. In the spectrum of GRB 240218A, we identified three sets of spectral transitions, Fe II, Zn II, and Cr II, originating from the ground state to the first excited state. These transitions have consistent column densities and ionization potentials. We measured the equivalent widths of these absorption lines (presented in Table B.1), noting that Zn II λ 2062 and Cr II λ 2062 are blended. To estimate their individual contributions, we first measured the total blend width ($EW = 7.68\text{\AA}$) and then apportioned contributions based on the oscillator strength ratios for Zn II and Cr II. The same procedure has been adopted for Zn II λ 2026 and Mg I λ 2026. Finally, we fit the CoG with free parameters for b and the column densities of Fe, Zn, and Cr using a uniform prior within a Monte Carlo Markov Chain (MCMC) sampling framework implemented in Python *emcee* package (Foreman-Mackey et al. 2013). For further details on the computational method, refer to de Wet et al. (2023). The results from the CoG supports and confirms the results obtained using Voigt Fit of absorption lines. The posterior distributions of all parameters derived from the MCMC procedure are shown in Figure B.1.

Table B.1: Rest frame Equivalent Widths of the identified absorption lines used to perform the curve of growth analysis.

Element	Transition	Observed Wavelength [\AA]	Equivalent Width (EW_r) [\AA]
Fe II	1608	12517.22	0.91 ± 0.09
Fe II	1611	12538.63	0.32 ± 0.03
Fe II	2260	17593.76	0.62 ± 0.07
Zn II	2026	15768.40	0.90 ± 0.08
Zn II	2062	16048.32	0.50 ± 0.09
Cr II	2056	16001.72	0.58 ± 0.06
Cr II	2062	16051.65	0.49 ± 0.08
Mg I	2026	15770.37	0.05 ± 0.01

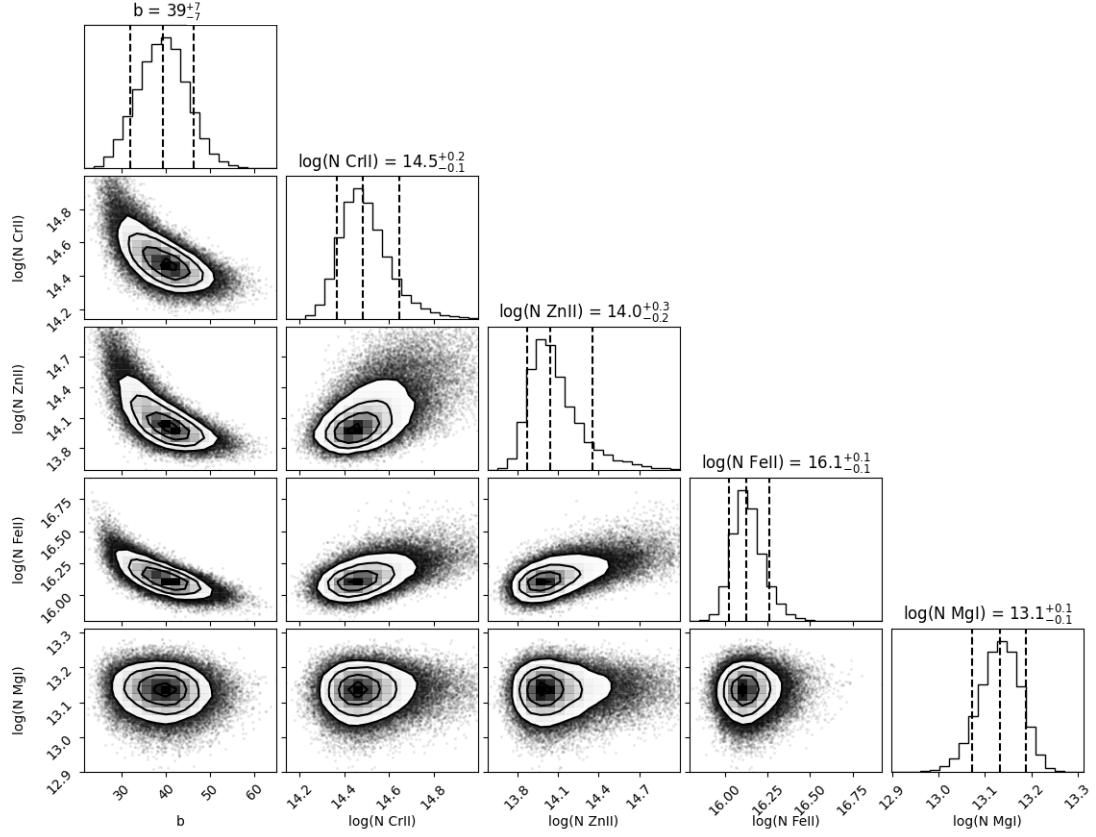


Fig. B.1: Corner plot showing the results of our MCMC parameter estimation. The histograms show the marginalized posterior densities for each parameter, while the two-dimensional projection reveal covariances. The best-fit parameters are indicated with black dashed lines (50th percentile). The uncertainties, shown also with black dashed lines, are computed as the 16th and 84th percentiles of the posterior samples along each axis, thus representing 1σ confidence ranges.

Appendix C: Nucleosynthesis and component-by-component analysis

We inspect also the $[X/Fe]$ residuals (over- and under-abundance of different elements with respect to iron i.e. after correcting for dust depletion), as shown in Figure C.1. They represent the deviations from the linear fits of Figure 4 which are likely due to the effects of nucleosynthesis, or peculiar abundances in the host ISM. The corresponding values and errors are reported in Table C.1. Given the small number of elements available we do not compare our results with nucleosynthetic models.

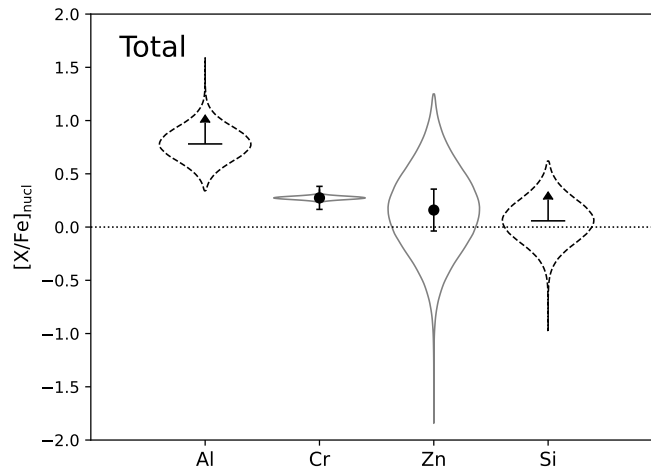


Fig. C.1: Abundances of different elements with respect to iron after correcting for dust depletion, for the total analysis. Limits are indicated by arrows and the error bars represent the uncertainty propagated from column density measurements; the violin plots represents the uncertainty caused by dust depletion estimated using one million Monte Carlo realizations of the $[Zn/Fe]_{fit}$.

Table C.1: $[X/Fe]$ residuals of the depletion pattern fitting (see Figures 4 and C.2). The values and uncertainties are obtained including MC simulations to take into account the dust depletion errors.

X	I	II	III	Tot
[Al/Fe]	$1.6^{+0.1}_{-0.1}$	$0.6^{+0.2}_{-0.2}$	$0.5^{+0.1}_{-0.1}$	$0.8^{+0.2}_{-0.2}$
[Cr/Fe]	$0.2^{+0.1}_{-0.1}$	$0.3^{+0.1}_{-0.1}$	$0.0^{+0.1}_{-0.1}$	$0.3^{+0.1}_{-0.1}$
[Zn/Fe]	$0.1^{+0.2}_{-0.2}$	$0.2^{+0.4}_{-0.4}$	$0.0^{+0.1}_{-0.1}$	$0.2^{+0.4}_{-0.4}$
[Si/Fe]	$0.7^{+0.1}_{-0.1}$	$0.2^{+0.2}_{-0.2}$	$-0.7^{+0.1}_{-0.1}$	$0.1^{+0.2}_{-0.2}$

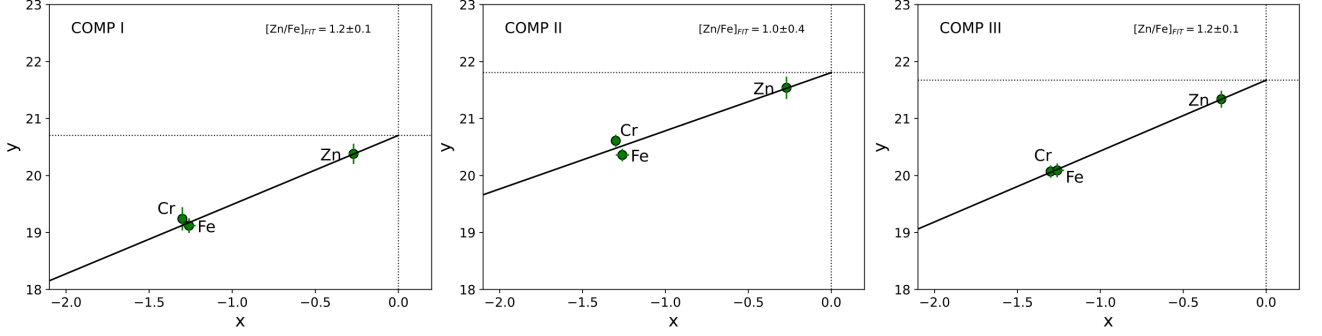


Fig. C.2: Similar to Figure 4, but for the individual components of the absorption-line profile. In this case y can be interpreted as an equivalent metal column (given that the information on the H I is not available)) and it is defined in detail in [Ramburuth-Hurt et al. \(2023\)](#). Again, the slope of the linear fit to the data (solid line) determines the overall strength of depletion $[Zn/Fe]_{fit}$, as labeled.

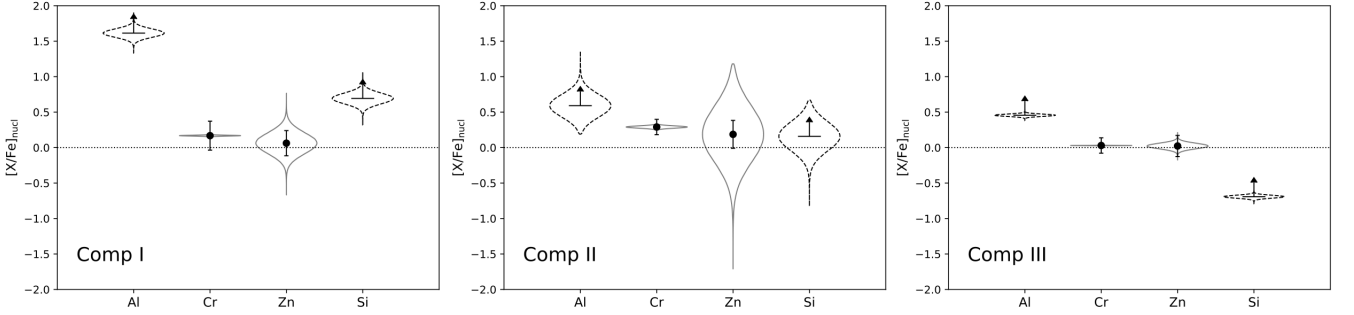


Fig. C.3: Same as Figure C.1 but for component-by-component analysis.